Nonlinear post-compression of a hybrid vortex mode in a gas-filled capillary

Mekha Vimal,[1] **Michele Natile,**[2] **Jean-François Lupi,**[3] **Florent Guichard,**[2] **Dominique Descamps,**[3] **Marc Hanna,**[1,*] **and Patrick Georges**[1]

[1]*Université Paris-Saclay, Institut d'Optique Graduate School, CNRS, Laboratoire Charles Fabry, 91127 Palaiseau, France*
[2]*Amplitude, 11 Avenue de Canteranne, Cité de la Photonique, 33600 Pessac, France*
[3]*Université de Bordeaux–CNRS–CEA, CELIA, UMR5107 Talence, France*
marc.hanna@institutoptique.fr

We demonstrate nonlinear temporal compression of a vortex beam by propagation in a gas-filled capillary. Starting from an ytterbium-based laser delivering 700 μJ 640 fs pulses at a 100 kHz repetition rate, the vortex beam is generated using a spiral phase plate and coupled to a capillary where it excites a set of four modes that have an overlap integral of 97% with a Laguerre–Gauss LG_{10} mode. Nonlinear propagation of this hybrid, orbital angular momentum (OAM)-carrying mode results in temporal compression down to 74 fs at the output. Beam and pulse characterizations are carried out to determine the spatial profile and temporal duration of compressed pulses. This result in multimode nonlinear optics paves the way towards the generation of OAM-carrying few-cycle pulses, isolated attosecond XUV pulses, and tunable UV pulses through resonant dispersive wave emission. © 2023 Optica Publishing Group

https://doi.org/10.1364/OL.506009

Introduction. The existence of orbital angular momentum (OAM) of light and its transfer from light to matter was first demonstrated three decades ago [1]. An azimuthally varying, quantized phase, $e^{i\ell\theta}$ is connected to photonic energy flow, implying a quantized, optical OAM in units of $\ell\hbar$. Such beams have a point of zero intensity in the transverse plane and are sometimes referred to as vortex beams. A natural basis for such beams are the Laguerre–Gaussian (LG) modes, in cylindrical coordinates

$$LG_{\ell p}(r, \theta, z) = LG_{00} L_p^{|\ell|} \frac{r^2}{w^2} \left(\frac{r}{w}\right)^{|\ell|} e^{-i(|\ell|+2p)\zeta-i\ell\theta}, \quad \textbf{(1)}$$

where LG_{00} is the Gaussian beam, $p \in \mathbb{N}$, $\ell \in \mathbb{Z}$, $w(z)$, and $\zeta(z)$ are the Gaussian beam radius and Gouy phase, and $L_p^{|\ell|}$ are generalized Laguerre polynomials.

Femtosecond vortex beams have been gaining interest in the ultrafast community, for instance, in atomic spectroscopy [2] and dichroism of chiral molecules [3,4]. To this end, the transfer of OAM from an infrared driver to the extreme ultraviolet through high harmonic generation was studied extensively [5,6]. Recent studies show the potential of OAM beams to study chiral and/or topological magnetic materials using helicoidal dichroism in the EUV and x ray domains [7].

Although structured light beams carrying OAM have been produced using optical elements like spiral phase plates (SPP) [8] for decades, these methods cannot be applied with few-cycle pulses because of chromatic effects. Another possibility to produce few-cycle vortices is to perform nonlinear temporal compression on a previously converted vortex beam, the generation of which would even allow the generation of isolated attosecond vortices [9]. In free-space post-compression setups, the use of vortex beams was studied theoretically [10,11] and demonstrated experimentally [12,13] both for multi-plate schemes and multipass cells, in the context of energy scaling. In setups using guiding structures, although vortex beams have been extensively studied in optical fibers [14], there has been no demonstration of post-compression in a gas-filled capillary with a vortex beam. However it has been achieved with radially polarized beams [15]. Several recent studies also point towards exploiting the nonlinear propagation of multimode [16] or higher-order mode [17] fields in such guiding structures, and the field of multimode nonlinear photonics is expanding rapidly [18].

In this Letter, we show that it is possible to perform nonlinear temporal compression on a set of capillary modes synthesizing an LG_{10} free-space mode. We first describe the hybrid OAM capillary modes to which an LG_{10} mode optimally couples before presenting the experimental results of spectral broadening with a guided vortex beam. This work paves the way to the generation of few-cycle OAM-carrying pulses, isolated attosecond vortices, and tunable deep and vacuum ultraviolet (V/DUV) OAM pulses through the resonant dispersive wave generation mechanism [19]. Using an optimized design based on a large core capillary, it could also be a technique for energy scaling of capillary-based compression setups.

The modes of a hollow-core capillary can be categorized into three families, namely the TE_{0m}, TM_{0m}, and EH_{nm} modes [20]. Similar to the case of optical fibers [14], it is possible to synthesize a field that is very close to an LG_{10} beam with linear polarization and a helical phase front by a linear combination of
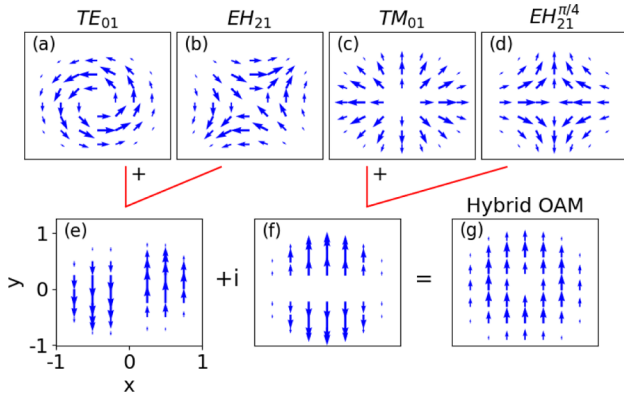
Fig. 1. Vector representation of the capillary modes that synthesize an OAM-carrying beam. Each vector represents qualitatively the intensity and direction of the electric field. (a)TE_{01}, (b)EH_{21}, (c)TM_{01}, (d) $EH_{21}^{\pi/4}$, (e) mode mixing of $TE_{01} + EH_{21}$, and (f) $TM_{01} + EH_{21}^{\pi/4}$. The two modes in (e) and (f) when added with a phase shift of $\pi/2$ yield the linearly polarized hybrid OAM mode (g).

the TE_{01}, TM_{01}, and EH_{21} modes, as illustrated in Fig. 1.

$$OAM = [TE_{01} + EH_{21}] + i \left[TM_{01} + EH_{21}^{\pi/4} \right]$$
$$OAM_x = 0 \tag{2}$$
$$OAM_y = 2J_1 \left(\frac{u_{11}r}{a} \right) e^{i\theta},$$

where J_1 is the first-order Bessel function of the first kind, $u_{11} \cong 3.83$ is its first zero, and a is the capillary radius. These capillary modes share the same propagation constant

$$\beta = \frac{2\pi}{\lambda} \sqrt{1 - \frac{1}{2} \left(\frac{u_{11}\lambda}{2\pi a} \right)^2}, \tag{3}$$

while their attenuation coefficient (α) depends on the nature of the mode.

$$\alpha = \left(\frac{u_{11}}{2\pi} \right)^2 \frac{\lambda^2}{a^3} \begin{cases} \dfrac{1}{\sqrt{\nu^2 - 1}}, & \text{for } TE_{01} \\[2mm] \dfrac{\nu^2}{\sqrt{\nu^2 - 1}}, & \text{for } TM_{01} \\[2mm] \dfrac{\frac{1}{2}(\nu^2 + 1)}{\sqrt{\nu^2 - 1}}, & \text{for } EH_{21} \end{cases} \tag{4}$$

where ν is the refractive index of the capillary glass and λ is the wavelength. Note that it is also possible to synthesize left- or right-circularly polarized LG_{10}-like modes using combinations of only two modes $EH_{21} + iEH_{21}^{\pi/4}$ or $TE_{01} + iTM_{01}$.

We now examine the coupling and propagation loss properties of the hybrid OAM mode. Figure 2(a) shows the overlap integral between this mode and a LG_{10} beam at its waist as a function of the waist size. For reference, the coupling of a Gaussian beam to the EH_{11} mode is also shown. The calculated optimal coupling efficiency is 97.2% for a waist radius equal to $0.56a$, to be compared to 98.1% for a waist radius of $0.64a$ in the Gaussian case. This shows that coupling to this hybrid mode can be almost as efficient as in the fundamental mode with a Gaussian beam. However, the coupling tolerance for variations in the spot size is lesser for the LG_{10} case, making it experimentally more difficult to achieve.
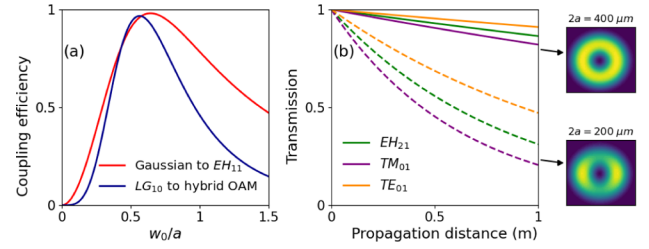

Fig. 2. (a) Coupling efficiency as a function of the ratio of beam waist w_0 to capillary core radius a between a perfect Gaussian beam and EH_{11} capillary mode (red) and between a LG_{10} beam and the hybrid OAM mode (blue). (b) Optical power transmission as a function of propagation distance for the four modes in a capillary of core diameter 400 μm (solid curves) and 200 μm (dashed curves), with the corresponding simulated intensity profiles at the output.

From Eqs. (3) and (4), we can see that the modes that contribute to the hybrid OAM mode are degenerate in propagation constant, but not in attenuation coefficients. This difference in propagation losses modifies the intensity, phase, and polarization state pattern of the hybrid OAM mode at the output. For example, in Fig. 2(b), we plot the transmission of the three modes for capillary core diameters of 400 and 200 μm, at a wavelength of 1.03 μm. Since the optical loss scale is set as $1/a^3$, they are both higher and spread over a larger relative interval for the smaller capillary. As a result, their effect on the beam output intensity profile is more visible when the core radius of the capillary is small, as also displayed in Fig. 2(b).

The OAM-carrying output field can be derived analytically by taking into account the different propagation losses. Simple algebra yields

$$|OAM_y(z)| = J_1 \left(\frac{u_{11}r}{a} \right) \left(e^{-\frac{X}{2}z} + e^{-\frac{X}{2}\nu^2 z} \right)$$
$$\times \sqrt{\cos^2 \theta \, e^{-Xz} + \sin^2 \theta \, e^{-X\nu^2 z}} \tag{5}$$

$$arg \left[OAM_y(z) \right] = \arctan \left(\tan \theta \, e^{-\frac{X}{2}(\nu^2 - 1)z} \right) \tag{6}$$

$$|OAM_x(z)| = J_1 \left(\frac{u_{11}r}{a} \right) \left(e^{-\frac{X}{2}\nu^2 z} - e^{-\frac{X}{2}z} \right)$$
$$\times \sqrt{\cos^2 \theta \, e^{-X\nu^2 z} + \sin^2 \theta \, e^{-Xz}} \tag{7}$$

$$arg \left[OAM_x(z) \right] = \arctan \left(\frac{1}{\tan \theta} \, e^{\frac{X}{2}(\nu^2 + 1)z} \right)$$
$$\text{with } X = \left(\frac{u_{11}}{2\pi} \right)^2 \frac{\lambda^2}{a^3} \frac{1}{\sqrt{\nu^2 - 1}}. \tag{8}$$

The deviation from the input in terms of intensity, phase, and polarization profiles increases as the core diameter decreases. But the fidelity of the output field is high in the case of high transmission, corresponding to most practical situations. This linear analysis of the modal properties leads us to use a capillary with a core diameter of 400 μm in the experiments.

The schematic of the experimental setup is show in Fig. 3. The experiment is carried out using a high-energy ytterbium-based femtosecond laser source (Tangor, Amplitude) delivering 700 μJ, 640 fs pulses at a central wavelength of 1030 nm, and a repetition rate of 100 kHz, corresponding to an average power of 70 W. The Gaussian spatial mode at the output of the laser is converted to a LG_{10}-like mode by introducing a SPP of topological charge $\ell = 1$ (VL-209-J-y-A, HOLO/OR) in the beam
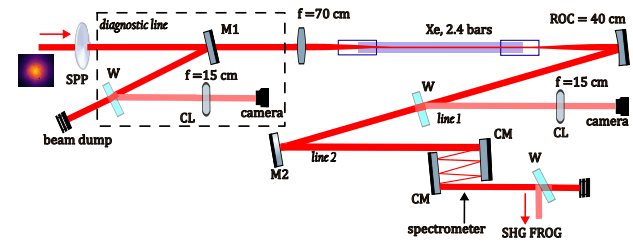
Fig. 3. Schematic of the experimental setup. SPP, spiral phase plate; M1, mirror 1 on flip mount; M2, mirror 2; W, glass wedge on flip mount; CL, cylindrical lens on flip mount; CM, chirped mirror.
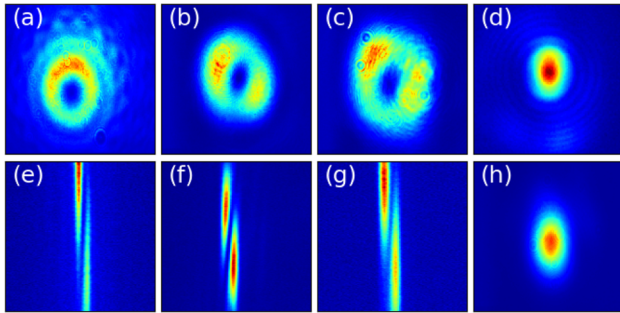

Fig. 4. Beam profile before (a) and after the capillary at 1 W input power (b) and 70 W input power (c). Near-field beam profile (d) of the reconverted Gaussian beam at the output. Astigmatic transformation pattern at the focus of the cylindrical lens for the input vortex beam (e) and the capillary output at 1 W input power (f) and 70 W input power (g). The single dark fringe and the similar tilt orientation in (e), (f), and (g) indicate that the OAM value $\ell = 1$ is conserved upon linear and nonlinear propagation. Beam profile at the capillary output for a Gaussian mode (h).

Fig. 5. Measured spectra at the output of the capillary when coupling Gaussian (red) and OAM-carrying beams (blue). The shaded region corresponds to the input spectrum.

path. Mirror M1 on a flip mount allows us to set up a diagnostic of the input beam. The beam reflected from M1 can be imaged onto a camera to view the far-field spatial profile of the beam after the SPP. For the spatial characterization of the beam and measurement of its OAM, we use the method of astigmatic transformation of the beam by a cylindrical lens [21–23]. The intensity pattern of a vortex beam acquires a form of fringes in the focal plane of a cylindrical lens. The number of dark fringes is equal to the modulus of the vortex topological charge, while the tilt indicates the charge sign. For this measurement, we insert a cylindrical lens (CL) with a focal length of 150 mm before the camera. Figure 4(a) shows the far-field image of the input beam and Fig. 4(e) the corresponding focal pattern of the cylindrical lens.

The LG_{10}-like mode thus generated is coupled into a hollow glass 1 m-long 400 μm-diameter capillary filled with Xenon gas at 2.4 bar. Beam coupling is achieved using the following procedure. Starting with a Gaussian beam (removing the SPP), we optimize coupling to the capillary using a waist radius around 0.64a. We then insert the SPP and find that this ensures reliable excitation of the hybrid OAM-carrying mode. This procedure results in a theoretical transmission of 51%, taking into account the imperfect coupling due to the non-optimal beam size, the fact that using a SPP with a Gaussian beam does not generate a perfect LG_{10} beam, and a theoretical transmission of 86% for the OAM-carrying hybrid mode. The measured overall (coupling and propagation) transmission in 2.4 bar Xe at maximum
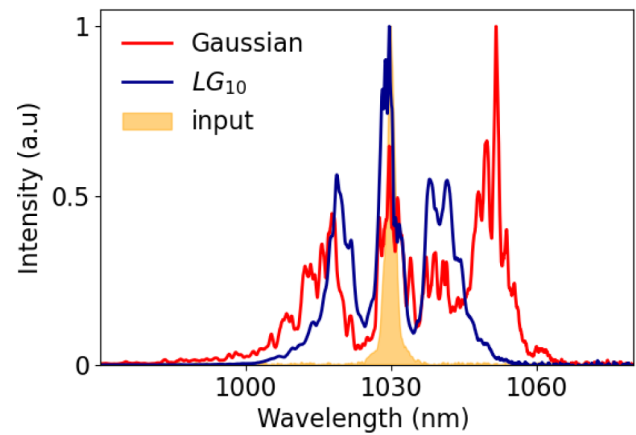
input power is 80% and 38% for the Gaussian and LG_{10} modes, respectively, with output powers of 56 W and 27 W.

The output beam is collimated with a spherical mirror and reflected from a glass wedge to the imaging camera (see *line 1* in Fig. 3). On the same line is mounted a cylindrical lens on a flip mount for spatial characterization of the output beam. Figures 4(b) and 4(c) show the output beam profiles and Figs. 4(f) and 4(g) the corresponding focal patterns of the cylindrical lens. The results show that the output beam has a LG_{10}-like intensity profile with topological charge $\ell = 1$, similar to the input both at low and high levels of nonlinearity. As an additional check, we reconvert the output vortex beam with an SPP with $\ell = 1$ at full power, before chirped mirrors. The obtained beam is shown after focusing by a f=150 mm lens in Fig. 4(d) and features a Gaussian profile, confirming that the vortex mode is preserved upon nonlinear propagation in the capillary at full energy. For comparison, the output of the capillary when coupling a Gaussian mode is shown in Fig. 4(h).

In order to remove the positive group delay dispersion (GDD) induced by the self-phase modulation accumulated during the nonlinear propagation in Xe-filled capillary, a set of chirped mirrors is used with a total GDD of -8550 fs^2 and >95% reflectivity. The spectral and temporal characterization of the compressed pulses is then performed at the output of chirped mirrors. The temporal profile of the pulse is measured with a Second Harmonic Generation Frequency Resolved Optical Gating apparatus (SHG-FROG). Figure 5 shows a comparison between the spectral broadening of Gaussian and LG_{10} spatial modes in the capillary at the maximum average power of 70 W and with 2.4 bar of Xe gas. The measured spectra correspond to Fourier-transform limited (FTL) pulses of 40 fs FWHM and 70 fs FWHM for the Gaussian and the LG_{10} mode, respectively, with a compression ratio that is 1.6 times higher for the Gaussian mode. This is in line with the fact that the effective area for the Gaussian and OAM-carrying beams can be approximated by $A_{\text{eff}}^G = \pi \times (0.64a)^2$ and $A_{\text{eff}}^{LG} = 2\pi \times (0.56a)^2$, yielding a ratio of approximately 1.5. The coupling efficiency and propagation losses also affect the compression ratio. Estimated values of B integral are 10 rad for the vortex beam and 17 rad for the Gaussian beam.

The FROG temporal characterization results of the compressed OAM-carrying pulse are shown in Fig. 6. The retrieved
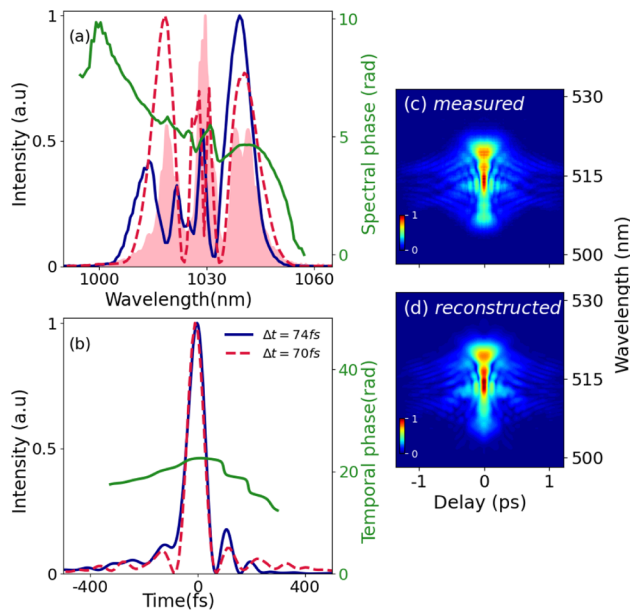
Fig. 6. Temporal characterization of the output compressed OAM-carrying pulses obtained with a capillary filled with 2.4 bar of Xe. (a) Spectral information. Shaded area: independently measured spectrum, blue curve: retrieved from FROG measurement, dashed red curve: simulation, green curve: spectral phase retrieved from FROG. (b) Temporal information. Blue curve: temporal intensity profile retrieved from FROG, dashed red curve: simulation. The legend shows the corresponding FWHM values. (c) Measured and (d) retrieved FROG traces.

spectrum matches well the independently measured spectrum. The FTL of the retrieved spectrum is 74 fs, very close to the pulse duration of 70 fs obtained from simulations. These numerical simulations solve the vectorial multimode nonlinear Schrödinger equation including losses, dispersion, self-phase modulation, self-steepening, and ionization-related effects. The FROG-measured input laser intensity and phase profiles are set as the input conditions. The simulated spectrum and compressed pulse intensity profile are plotted in Fig. 6, with features in good agreement with the experimental FROG result. The energy contained in the main temporal lobe is estimated to be 200 µJ, 72% of the total available energy at the output.

In summary, we have demonstrated nonlinear post-compression of a hybrid vortex beam in a gas-filled capillary at a pulse energy level of 700 µJ. The spatial intensity and phase profile of the vortex beam are conserved upon nonlinear propagation while ensuring a compression ratio of 9 for the chosen experimental parameters. This confirms the robust nature of the hybrid capillary mode for carrying a topological charge. In the near future, such a setup combined with a first nonlinear pulse compression stage based on multipass cell could become a robust source for applications requiring few-cycle pulses carrying an OAM.

Disclosures. The authors declare no conflicts of interest.

Data availability. Data underlying the results presented in this article are not publicly available at this time but may be obtained from the authors upon reasonable request.

REFERENCES

1. L. Allen, M. W. Beijersbergen, R. Spreeuw, *et al.*, Phys. Rev. A **45**, 8185 (1992).
2. G. De Ninno, J. Wätzel, P. R. Ribič, *et al.*, Nat. Photonics **14**, 554 (2020).
3. J.-L. Bégin, A. Jain, A. Parks, *et al.*, Nat. Photonics **17**, 82 (2023).
4. W. Brullot, M. K. Vanbel, T. Swusten, *et al.*, Sci. Adv. **2**, e1501349 (2016).
5. G. Gariepy, J. Leach, K. T. Kim, *et al.*, Phys. Rev. Lett. **113**, 153901 (2014).
6. R. Géneaux, A. Camper, T. Auguste, *et al.*, Nat. Commun. **7**, 1 (2016).
7. M. Fanciulli, M. Pancaldi, E. Pedersoli, *et al.*, Phys. Rev. Lett. **128**, 077401 (2022).
8. M. Massari, G. Ruffato, M. Gintoli, *et al.*, Appl. Opt. **54**, 4077 (2015).
9. G. Sansone, E. Benedetti, F. Calegari, *et al.*, Science **314**, 443 (2006).
10. L. Xu, D. Li, J. Chang, *et al.*, Phys. Rev. A **106**, 053516 (2022).
11. H. Cao, R. S. Nagymihaly, and M. Kalashnikov, Opt. Lett. **45**, 3240 (2020).
12. B.-H. Chen, H.-W. Huang, R.-S. Ye, *et al.*, Opt. Lett. **47**, 4423 (2022).
13. M. Kaumanns, D. Kormin, T. Nubbemeyer, *et al.*, Opt. Lett. **46**, 929 (2021).
14. S. Ramachandran and P. Kristensen, Nanophotonics **2**, 455 (2013).
15. F. Kong, H. Larocque, E. Karimi, *et al.*, Optica **6**, 160 (2019).
16. R. Safaei, G. Fan, O. Kwon, *et al.*, Nat. Photonics **14**, 733 (2020).
17. C. Brahms and J. C. Travers, J. Phys. Photonics **4**, 034002 (2022).
18. L. G. Wright, W. H. Renninger, D. N. Christodoulides, *et al.*, Optica **9**, 824 (2022).
19. C. Brahms, D. R. Austin, F. Tani, *et al.*, Opt. Lett. **44**, 731 (2019).
20. E. A. Marcatili and R. A. Schmeltzer, Bell Syst. Tech. J. **43**, 1783 (1964).
21. J. Serna, F. Encinas-Sanz, and G. Nemes, J. Opt. Soc. Am. A **18**, 1726 (2001).
22. V. Denisenko, V. Shvedov, A. S. Desyatnikov, *et al.*, Opt. Express **17**, 23374 (2009).
23. H. T. Nguyen, G. Stepniewski, A. Filipkowski, *et al.*, Opt. Express **30**, 45635 (2022).